



ELSEVIER

Available online at [www.sciencedirect.com](http://www.sciencedirect.com)

SCIENCE @ DIRECT®

Vacuum 80 (2006) 621–630

VACUUM  
SURFACE ENGINEERING, SURFACE INSTRUMENTATION  
& VACUUM TECHNOLOGY

[www.elsevier.com/locate/vacuum](http://www.elsevier.com/locate/vacuum)

Short communication

# Integrated plasma-aided nanofabrication facility: Operation, parameters, and assembly of quantum structures and functional nanomaterials

S. Xu<sup>a</sup>, K. Ostrikov<sup>a,b,\*</sup>, J.D. Long<sup>a</sup>, S.Y. Huang<sup>a</sup>

<sup>a</sup>*Plasma Sources and Applications Center, NIE, Nanyang Technological University, 637616 Singapore, Singapore*

<sup>b</sup>*School of Physics, The University of Sydney, Sydney, NSW 2006, Australia*

Received 24 May 2005; received in revised form 15 July 2005

## Abstract

The development, operation, and applications of two configurations of an integrated plasma-aided nanofabrication facility (IPANF) comprising low-frequency inductively coupled plasma-assisted, low-pressure, multiple-target RF magnetron sputtering plasma source, are reported. The two configurations of the plasma source have different arrangements of the RF inductive coil: a conventional external flat spiral “pancake” coil and an in-house developed internal antenna comprising two orthogonal RF current sheets. The internal antenna configuration generates a “unidirectional” RF current that deeply penetrates into the plasma bulk and results in an excellent uniformity of the plasma over large areas and volumes. The IPANF has been employed for various applications, including low-temperature plasma-enhanced chemical vapor deposition of vertically aligned single-crystalline carbon nanotips, growth of ultra-high aspect ratio semiconductor nanowires, assembly of optoelectronically important Si, SiC, and  $\text{Al}_{1-x}\text{In}_x\text{N}$  quantum dots, and plasma-based synthesis of bioactive hydroxyapatite for orthopedic implants.

© 2005 Elsevier Ltd. All rights reserved.

**Keywords:** Plasma processing and deposition; Nanostructures; Biomaterials; Quantum effects

## 1. Introduction

Plasma-assisted chemical vapor deposition (PECVD) systems have recently been widely

employed for the fabrication of various nanostructures and nanostructured materials owing to the unique ability of the plasma to dissociate and activate complex gaseous molecular matter. Moreover, reactive plasmas can sustain gas-phase polymerization of various macromolecules, long polymeric chains and rings, nano-sized clusters, and nucleates; the latter can evolve into larger

\*Corresponding author. Tel.: +61 293 516 081; fax: +61 29351 7762.

E-mail address: [K.Ostrikov@physics.usyd.edu.au](mailto:K.Ostrikov@physics.usyd.edu.au) (K. Ostrikov).

agglomerates and nucleates. Due to the overwhelming complexity of the numerous elementary processes in the gas phase (which sometimes includes several hundreds of reactive species), the ability to manipulate the number densities, energies, and fluxes of the entire range (from atoms and simple ions to macromolecules and nucleates) of the plasma species becomes a critical issue of plasma processing [1–5]. Indeed, it has been frequently observed that if the process parameters (in the plasma and on the surface) are not chosen properly, characteristics of the resulting films and materials do not meet the expected industrial quality standards. This is particularly the case in nanofabrication of epitaxial films and functional nanostructures.

To address this issue, one needs to tailor the elementary gas-phase and surface kinetics and chemistry, which ultimately leads to greater control and predictability of various low-temperature plasma-assisted industrial processes. It is therefore very important to develop the plasma source and process specifications that can be used for the above purpose. Here, we report on the development and potential industrial applications of two configurations of the multi-purpose integrated plasma-aided nanofabrication facility, whereby high-density, low-pressure, inductively coupled plasma can be used for the PECVD combined with the RF sputtering of multiple solid targets.

## 2. Experimental

A schematic diagram of the IPANF for the generation of reactive plasmas is shown in Fig. 1. This device encompasses the means of generation of highly uniform high-density plasmas by driving the external spiral [the RF coil shown in Fig. 1(a)] or internal [Fig. 1(b)] oscillating unidirectional RF currents, operation of low-pressure discharges in mixtures of reactive gases, control of deposition processes by using the substrate holders with the temperature- and deposition area-control functions, multiple RF sputtering targets [two of them are shown in Fig. 1(a)], and advanced diagnostic instrumentation. The internal RF coil can be installed by replacing the top quartz window [that

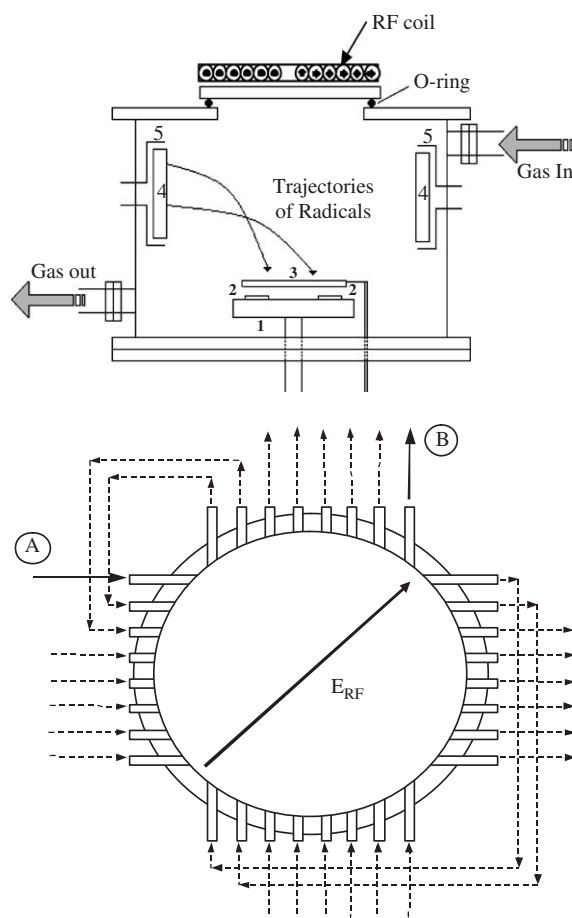


Fig. 1. Schematics of the plasma reactor (upper figure). Here, (1) substrate holder; (2) substrates; (3) shutter; (4) target; (5) target holder/electrode. Alternative configuration for the top section of the chamber (lower figure). Here, A and B denote the antenna connection points to the RF generator.

separates the vacuum chamber and the RF coil in Fig. 1(a)] by the top section of the chamber, the top view of which is shown in Fig. 1(b). To enable future large-area and large-volume industrial plasma processing, the internal diameter of the discharge chamber has been up-scaled from 32 cm [6] to 50 cm. The new vacuum vessel is equipped with the external (flat spiral “pancake”) or internal (two orthogonal RF current sheets) inductive coils (antennas) where the RF current is driven by a 460 MHz RF generator through a matching network. The exact ranges of RF input power

(typically in the range between 100 W and 3 kW) and parameters of the RF circuit to sustain the discharges in the required gas feedstock and working pressure (usually in the 0.07–26.3 Pa range) are estimated by using results of our previous numerical simulations of various RF discharges sustained in chemically active gases [7–9].

To enable the efficient deposition of various thin films in the temperature-controlled regime, the moveable (in the vertical and azimuthal directions) substrate stage with a built-in thermocouple and external temperature control unit, is installed as shown in Fig. 1. An automated shutter (with or without any perforated pattern) enables one to partially cover any part of the surface being processed and control (e.g. focus) the ion/neutral fluxes from the plasma. Three equidistantly positioned (along the circumference of the chamber) RF magnetron sputtering electrodes (selectively powered with RF pulses with the preset pulse durations and “pulse-offs”) enable the sequential and controllable release of various sputtered material (e.g. Al, Fe, Ni, Co, In, Si, Ti, etc.) into the reactive gas environment. This technique is particularly useful in the plasma-assisted synthesis of various semiconductor quantum confinement structures and bio-compatible films, as shown in the next section. The advanced plasma diagnostic instrumentation includes Langmuir and magnetic probes, ultra-high-resolution optical emission spectroscopy (OES), and quadrupole mass spectrometry (QMS) [6,10,11].

Global plasma parameters were obtained from the time-resolved measurements by a single RF-compensated cylindrical Langmuir probe (LP). The probe was powered by AC (50 Hz) AC voltage in the range from –40 to +40 V through a variable transformer. To isolate the electric connection between the probe and main power supply an additional isolation transformer (with 1:1 ratio) was used. The probe voltage across the plasma load resistance was measured by a Tektronix voltage probe and monitored on a digital storage oscilloscope (Tektronix model 380) via a 1.0 MHz low-pass filter. The probe current was obtained by measuring the voltage drop across a  $0.26\ \Omega$  resistor and monitored on the same oscilloscope via a

0.2 MHz low-pass filter. All the obtained signals were transmitted to a PC via the GPIB port of the oscilloscope. A PC-based data acquisition system was used to record and process the data and obtain the electron density, effective electron temperature, plasma potential, and electron energy distribution/probability functions (EEDF/EEPF).

The main plasma parameters were determined by using the second derivative of the Langmuir probe current–voltage characteristics (Druyvestein routine) [12]. We note that the reproducibility of the data collected in the experiments of our interest here was excellent. Since the plasma chamber provides a good reference ground for the single RF-compensated LP measurements in the electron collection voltage range, the plasma potential and effective electron temperature can be accurately obtained from the measured  $I$ – $V$  probe characteristics. The plasma density  $n_e$ , effective electron temperature  $T_e$ , and plasma potential  $V_p$  were determined by using the Druyvestein routine [12]. In particular,  $n_e$  and  $T_e$  can be expressed as

$$n_e = \int g_e(V) dV,$$

$$T_e = \frac{2}{3n_e} \int V g_e(V) dV,$$

and the electron energy distribution function  $g_e(V)$  can be obtained through the second derivative of the probe current over the voltage  $d^2 I_e/dV^2$  as

$$g_e(V) = \frac{2m_e}{e^2 A} \left( \frac{2eV}{m_e} \right)^{1/2} \frac{d^2 I_e}{dV^2},$$

where  $e$ ,  $m_e$ , and  $A$  are the elementary charge, electron mass, and the probe surface area. The plasma potential  $V_p$  can be found as the maximum of the first derivative of the dependence  $I(V)$  or as the zero crossing point of the second derivative of the probe current [12].

Physically, the integrated plasma facility of our interest here combines the best features of the inductively coupled plasma source and RF magnetron-sustained plasmas. As can be seen from Fig. 2, the IPANF plasma features high density  $n_e$  (exceeding  $5 \times 10^{12}\ \text{cm}^{-3}$  at moderate RF power densities) common for external flat spiral inductive coil configurations [6,10] and a notable uniformity

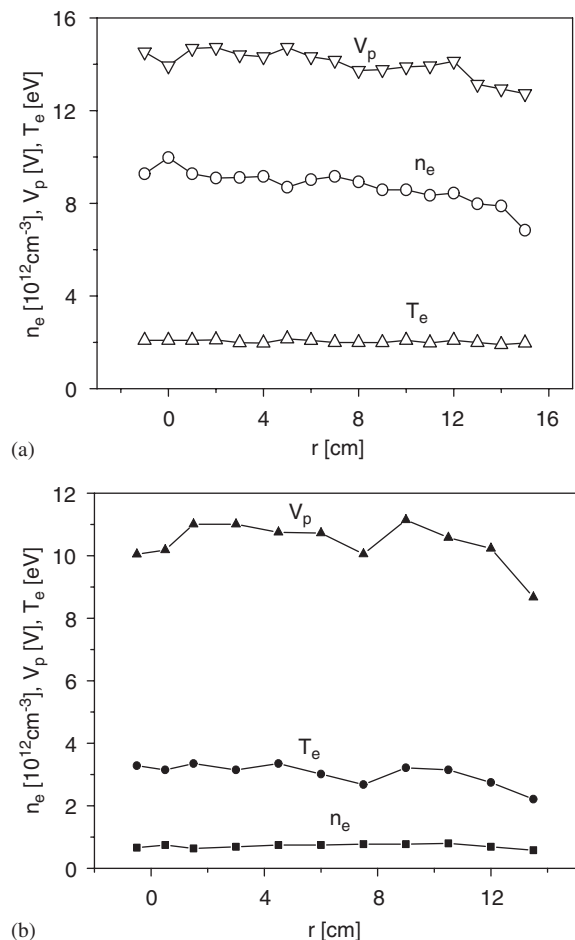


Fig. 2. Spatial profiles of the argon plasma density  $n_e$ , electron temperature  $T_e$  and plasma potential  $V_p$  in the two configurations of the IPANF: (a) with external flat spiral inductive coil (input power  $P_{\text{in}} = 1.1$  kW, gas pressure  $p_0 = 2.93$  Pa); (b) with internal (two orthogonal RF current sheets) inductive coil ( $P_{\text{in}} = 0.78$  kW,  $p_0 = 4$  Pa).

of the plasma parameters over large surface areas and discharge volumes, peculiar for RF plasma sources with internal oscillating currents [13]. Moreover, the magnetic probe measurements reveal a deep penetration of RF magnetic fields in the chamber [11]. In the combined PECVD + sputtering operation mode, the above features are complemented by a controllable release of solid-phase material via the magnetron sputtering of multiple targets [14,15].

The optical emission spectra were collected in the wavelength range of 300–900 nm by using the optical emission spectroscopy measurement system. The variation of the optical emission intensity of different atomic, ionic, molecular, or radical lines in the plasma can be monitored in real time. The optical emission of different spectral lines of the excited/ionized species produced by the plasma discharge is collected by a collimated optical probe inserted radially or axially into the plasma chamber. An optical fiber is used to transmit the collected signal to the entrance slit of a monochromator (Acton Research SpectraPro-750i model, 0.750 m Focal Length Triple Grating Imaging Monochromator/Spectrograph). The emission is amplified by a photomultiplier (PMT, THORN EMI electron tube) and then dispersed and analyzed by a monochromator (with spectral resolution of 0.023 nm) in the preset wavelength range. The amplitude of the output signal from the photomultiplier could be changed by adjusting the voltage output from a high-voltage generator. In order to monitor the output signal on the computer in real time, the signal is continuously digitized by an A/D converter built-in in the scan controller. The scanning and data acquisition process was controlled by the data acquisition and analysis software Spectrasense<sup>TM</sup> (Acton Research Corporation). Using the data acquisition system, one can record broad spectral bands or selectively monitor certain spectral lines. Fig. 3(a) shows representative optical emission spectra of neutral species in the process of argon plasma-assisted RF magnetron sputtering deposition of biocompatible hydroxyapatite films discussed in more detail in the following section.

Quadrupole mass spectrometry (QMS) is used for real-time in situ diagnostics of neutral species in the gas phase of the discharge. The IPANF facility is equipped with a quadrupole mass analyzer system Microvision Plus manufactured by MKS Instrument Spectra Products. This system enables one to measure number densities of neutral species with atomic masses not exceeding 200 amu. The spectrometer consists of an ionization chamber, a quadrupole analyzer, a pumping system, and a control unit. The entire measurement process is computer-controlled. The

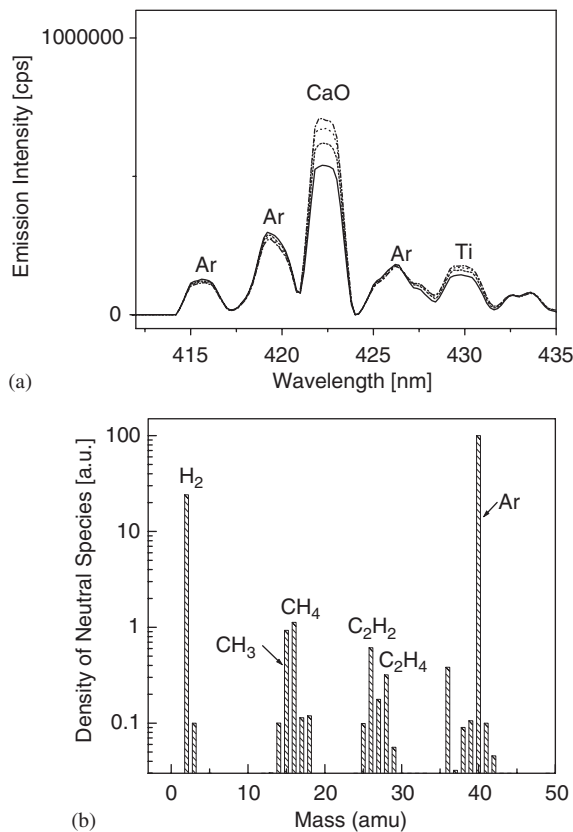


Fig. 3. Optical emission (a) and quadrupole mass spectrometry (b) spectra recorded during two different nanofabrication processes described in Section 3 (IPANF configuration with the external flat spiral RF antenna). (a) refers to the RF magnetron sputtering deposition of nanocrystalline hydroxyapatite bioceramics, whereas (b) refers to the PECVD of single-crystalline carbon nanotip microemitter structures. Process parameters: (a) HA sputtering in argon; RF power and working gas inlet are 700 W and 120 sccm, respectively. Solid, dashed, dotted, and dash-dotted lines correspond to the following values of DC bias voltage: 0, -75, -150, and -200 V, respectively; (b) Ar(35.2 sccm) + CH<sub>4</sub>(12.5 sccm) + H<sub>2</sub>(8 sccm) gas mixture,  $P_{in} = 2.17$  kW, substrate bias and temperature -300 V and 300 °C, respectively.

quadrupole mass analyzer is connected to the vacuum chamber with a 23 cm long,  $\phi 24$  mm metallic tube. Gas species are first ionized in the ionization chamber and then analyzed by a mass detector. Partial pressures of different species are usually recorded as intensities of ion fluxes in the detector. A Faraday cup with a single filter is used

as the ion detector. The sensitivity of the Faraday cup detector is in the range of  $7.5\text{--}75 \times 10^{-7}$  A/Pa, which allows one to process the output signals from the detector without any additional amplification. Data acquisition is controlled by a multipurpose Process Eye 2000 software, which enables the user to monitor, in real-time, density variations of a selected species or scan any preset mass ranges below 200 amu. The results of the QMS of Ar + H<sub>2</sub> + CH<sub>4</sub> plasmas in the process of nanoassembly of single-crystalline carbon microemitter structures are displayed in Fig. 3(b). In particular, the QMS results allow one to identify the main reactive species that may be responsible for the assembly of the carbon nanotip structures. In particular, one can notice a remarkable abundance of the reactive neutral radical CH<sub>3</sub>, which, in addition to the reactive cation CH<sub>3</sub><sup>+</sup> has been proposed as a potential building block of the microemitter structures in question [17]. More details about the growth mechanism of such nanostructures are given in Section 3.

To conclude this section, we note that further details of the plasma source operation, stability, plasma diagnostics, and parameters (mostly relevant to the prototype versions of the IPANF) can be found elsewhere [6,10,11].

### 3. IPANF: applications

The aim of this section is to demonstrate successful applications of the IPANF for fabrication of vertically aligned carbon nanotip structures, semiconductor quantum dots and nanowires, and hydroxyapatite (HA) biocompatible coating. As we have mentioned in Section 2, we have used the low-to-intermediate pressure (0.07–26.3 Pa) discharges in reactive gas mixtures specified in each particular case. We emphasize that results of the plasma diagnostics described in Section 2 are complemented by the numerical modeling of the particle and power balance in the reactive plasma environment, which enables us to estimate fluxes and energies of the reactive plasma species (e.g. radical cations, neutral radicals, charged and neutral clusters, and nucleates) during



their deposition onto the substrate. The synthesized films were characterized by means of the atomic force microscopy (AFM), high-resolution transmission electron microscopy (HRTEM), field emission scanning electron microscopy (FESEM), X-ray diffractometry (XRD), and other advanced analytical techniques.

Examples of functional nanofilms and nanostructures synthesized in the IPANF are shown in Fig. 4. We now discuss process conditions and physics involved in each particular case shown in Fig. 4. Fabrication of vertically aligned carbon-based nanostructures requires the PECVD of carbon material onto catalyzed (e.g. Co, Ni)

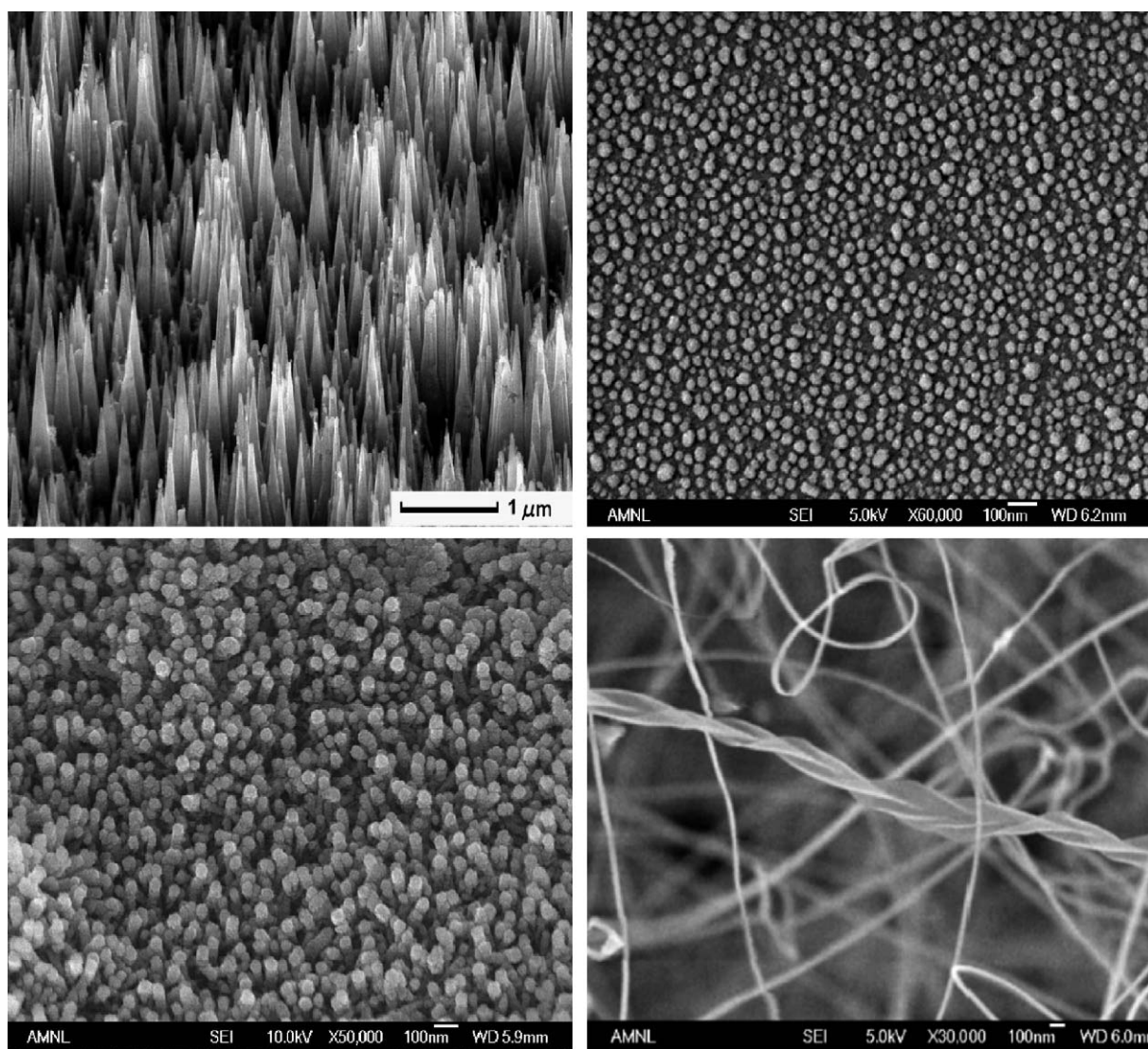


Fig. 4. Various functional nanofilms and nanostructures fabricated in the IPANF. Clockwise from top left: carbon nanotip arrays grown by low-pressure PECVD in Ar + CH<sub>4</sub> + H<sub>2</sub> plasmas; large-area patterns of Al<sub>x</sub>In<sub>1-x</sub>N quantum dots synthesized by sputtering of Al and In targets in low-pressure Ar + N<sub>2</sub> plasmas; ultra-high aspect ratio AlN quantum wires grown in the IPANF by sputtering of Al targets in Ar + N<sub>2</sub> plasmas; surface morphology of HA crystalline grown from simulated body fluid on the CaPTi thin film deposited by the RF magnetron sputtering of HA and Ti targets in low-pressure Ar plasmas.

silicon substrates. The low-pressure RF plasma discharges are sustained in the  $\text{Ar} + \text{CH}_4/\text{C}_2\text{H}_2 + \text{H}_2$  mixtures, where hydrogen is used to activate the catalyst surface and methane or acetylene serve as carbon source gases. The process of carbon nanostructure fabrication critically depends on plasma parameters (e.g. species number densities and fluxes, electron temperature, etc.), temperature, and DC bias of the substrate stage. The vertically aligned carbon nanotip structures shown in Fig. 4 show current densities of field emission exceeding  $3 \text{ mA/cm}^2$  at low emission threshold fields  $\sim 6.5 \text{ V}/\mu\text{m}$ , and are promising for the development of microemitter arrays for large-area display panel devices.

Fig. 5 illustrates growth kinetics of carbon nanotip structures of our interest here. During the first stage [Fig. 5(i)], argon ions are used for surface conditioning. The combined effect of substrate heating and nickel catalyst etching by atomic hydrogen results in fragmentation of the catalyst nanolayer as shown in Fig. 5(ii). When a carbon-bearing gas ( $\text{CH}_4$  in case of single-crystalline carbon nanotip arrays and  $\text{C}_2\text{H}_2$  in case of carbon nanowall-like structures) is introduced, a large amount of reactive cationic  $\text{CH}_3^+$  and neutral  $\text{CH}_3$  species is created, as confirmed by the OES and QMS diagnostic techniques. In our experiments with moderately biased substrates (up to  $\sim -300 \text{ V}$ ), the fluxes of cationic species onto the surface exceed those of neutral radicals [9]. Furthermore, recent ab initio Density Functional Theory [16] computations of stable chemical configurations of hydrogen-terminated carbon nanotip structures and Monte Carlo simulations of microscopic ion fluxes on the nanotip surfaces [17] suggest the crucial role of the cationic  $\text{CH}_3^+$  and neutral  $\text{CH}_3$  radicals as building blocks of single-crystalline vertically aligned carbon nanotip structures. Fig. 5(iii) depicts the next stage of the nanotip growth, when the  $\text{CH}_3^+$  cations incorporate into the growing structure forming hydrogen-terminated carbon networks. Meanwhile, atomic hydrogen, another important working unit, continues to etch continuously precipitating disordered carbon phase, giving rise to sharp carbon nanotip structures [Fig. 5(iv)]. Details of the PECVD of other carbon-based nanostructures in

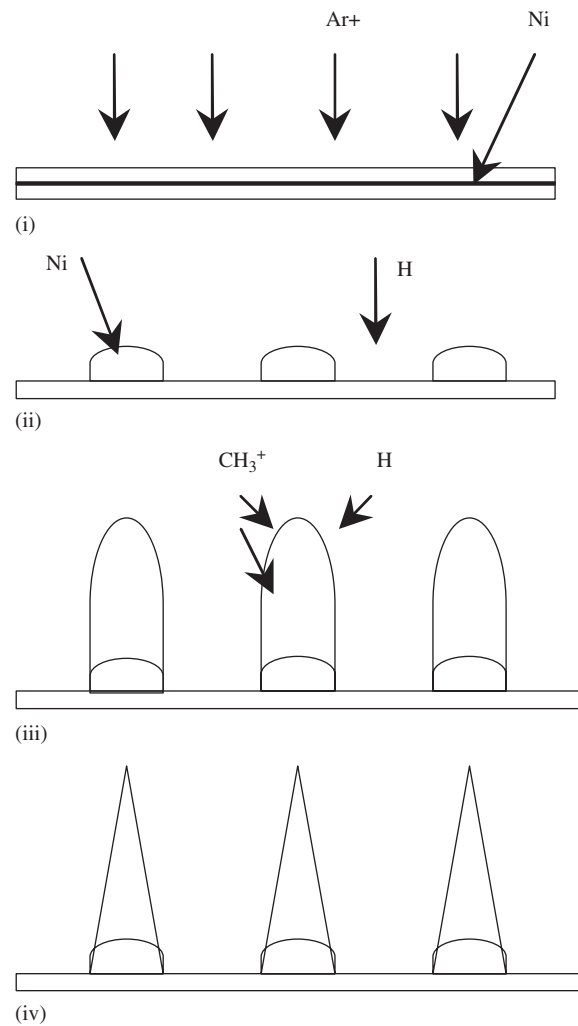


Fig. 5. Growth kinetics of single-crystalline carbon nanotips from  $\text{Ar} + \text{H}_2 + \text{CH}_4$  plasmas generated in the IPANF.

different deposition regimes can be found elsewhere [9,18,19].

For the fabrication of the size-selective quantum dot (QD) arrays, small lattice constant mismatch and wider energy gap buffer layers have been developed on the deposition substrates. A wide-bandgap AlN (6.2 eV) is used as a buffer layer (and also electron confining layer) for the fabrication of  $\text{Al}_x\text{In}_{1-x}\text{N}$  QD patterns shown in Fig. 4. The synthesis of  $\text{Al}_x\text{In}_{1-x}\text{N}$  QD structures proceeds as follows. First, Si(100) substrates with the surface

area of  $\sim 2\text{--}3\text{ cm}^2$  are conditioned in 2.63 Pa Ar plasma sustained with  $\sim 0.7\text{ kW}$  RF powers in the flat external spiral inductive coil mode of the IPANF. After letting in a similar (2–3 Pa partial pressure) amount of the  $\text{N}_2$  precursor gas and applying a 13.56 MHz RF power (typically 100–200 W) to one of the RF sputtering electrodes with the high-purity (99.9%) aluminum target, one can deposit a thin (a few nm) AlN buffer layer. Second, the ternary  $\text{Al}_x\text{In}_{1-x}\text{N}$  quantum dot structures are deposited by co-sputtering of high-purity Al and In solid targets. The values of  $x$  (which is the energy bandgap dependent) can be controlled by the deposition conditions, in particular, by the RF power supplied to the Al sputtering target. Once optimized, large-area  $\text{Al}_x\text{In}_{1-x}\text{N}$  quantum dot patterns (Fig. 4) can be fabricated. A similar procedure can be employed for the assembly of Si or SiC QDs by using  $\text{CH}_4$  and  $\text{SiH}_4$  as reactive gases and/or SiC as a sputtering target. SiC quantum dot structures exhibit pronounced size-dependent photoluminescence properties as can be seen in Fig. 6. Indeed, the maximum intensity of the room-temperature photoluminescence is observed at  $\lambda \sim 670\text{ nm}$  for the median QD size of 12 nm (curve 1) and is shifted towards longer wavelengths  $\lambda \sim 715\text{ nm}$  (curve 2) and  $\lambda \sim 750\text{ nm}$  (curve 3) when the QD size becomes larger (20 and 35 nm for curves 2 and

3, respectively). Interestingly, at higher substrate temperatures ( $\sim 550^\circ\text{C}$ ) and higher RF power ( $\sim 0.5\text{ kW}$ ) applied to the Al sputtering target, one can synthesize ultra-high aspect ratio AlN nanowires shown in the bottom right SEM micrograph in Fig. 4.

The deposition of biocompatible calcium phosphate-based films requires the concurrent/phase-in RF magnetron sputtering of hydroxyapatite and titanium targets in the low-to-intermediate pressure discharges in Ar (gas) +  $\text{H}_2\text{O}$  (liquid) feedstock in which  $\text{H}_2\text{O}$  plays a critical role in the enhancement of hydroxylation (hence, biocompatibility) of the bioceramic films. The bio-inert Ti6Al4V orthopedic material widely used for hip joint implants is used as a host matrix. The substrate bias and distance from the sputtering targets, the partial pressures of the gas mixture, and RF power supplied to the sputtering electrode can be independently adjusted to achieve the required film parameters. In particular, by sputtering the Ti target, one can achieve the acceptable industrial standards for the interface bonding strength [15,20,21]. On the other hand, by varying the (negative) bias, one can control the elemental presence and crystallinity in films. Combined in situ OES and QMS measurements suggest that the presence of calcium in the film is controlled by  $\text{CaO}^+$  cations, whereas the presence of phosphorus by the  $\text{PO}_4^{3-}$  anions. Films feature excellent biocompatibility and sustain an efficient in growth of HA material from the simulated body fluid, which is depicted in the bottom left SEM micrograph in Fig. 4. Amazingly, the films feature excellent crystallinity even after 168 h of immersion in a simulated body fluid environment, as can be seen in Fig. 7. We note that the RF magnetron sputtering technique enables one to generate smaller (small nanoclusters and neutral, cationic, and anionic radicals) building blocks compared to commonly used plasma-assisted spraying of micron-sized HA powders. Physically, subnanometer- and nanometer-sized building blocks are much more efficiently recrystallized upon deposition as they easily fit (radicals) or adopt (nanoclusters) the crystalline structure of the film grown, which explains the results shown in Fig. 7.

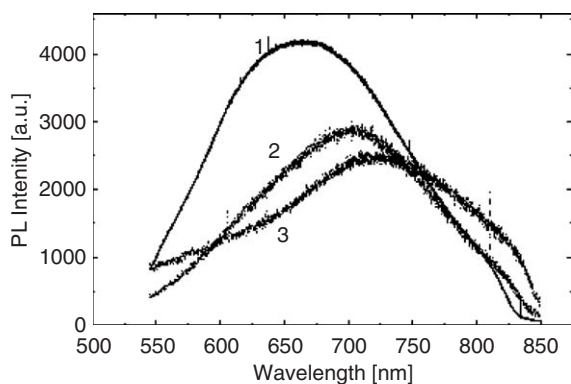


Fig. 6. Size-dependent intensity of room-temperature photoluminescence of SiC quantum dots assembled in Ar +  $\text{SiH}_4$  +  $\text{CH}_4$  plasmas on a preformed AlN buffer nanolayer. Curves 1–3 correspond to the median (over the SEM scanning area) quantum dot sizes of 12, 20, and 35 nm, respectively.



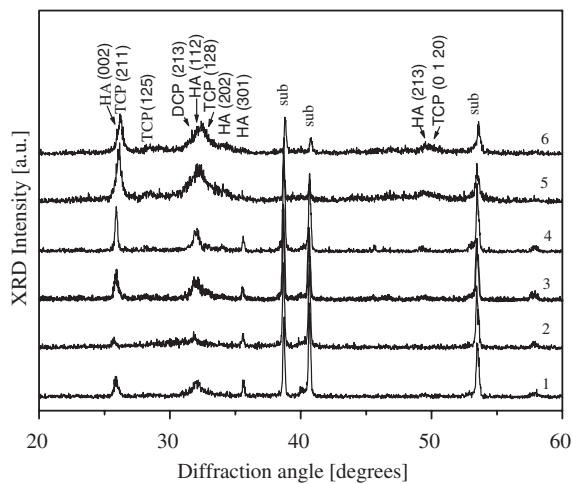


Fig. 7. XRD spectra of hydroxyapatite bioceramic films synthesized in the IPANF by concurrent sputtering of HA and Ti targets in Ar plasmas versus duration of their immersion in a simulated body fluid. Curves 1–6 correspond to as-grown films, and films immersed in the SBF for 6, 12, 24, 48, and 168 h, respectively.

#### 4. Concluding remarks

In this article, we have reported on the development, operation modes, and parameters of the integrated plasma-aided nanofabrication facility that comprises means of generating high-density reactive gaseous and metal plasmas by using a combination of the external and internal inductive coils with independently powered RF magnetron sputtering electrodes. This multi-option facility has been successfully used for the synthesis of various nano- and biomaterials, including, but not limited to, single-crystalline carbon microemitters, various carbon-based nanostructures, AlN,  $\text{Al}_x\text{In}_{1-x}\text{N}$ , and SiC quantum dot arrays, ultra-high aspect AlN nanowires, and nanocrystalline hydroxyapatite bioceramic coatings with tunable bioresponse.

Our future efforts will be focused on the achievement of thin film parameters complying with the relevant industry standards, analysis of the film microstructure (sizes and shapes of morphology elements, micro- and nano-structure, crystal structure, grain size, etc.), and numerical investigation of the relation of the film parameters,

and the composition/fluxes of the reactive plasma species and process conditions, such as RF power, gas composition, working pressure, bias voltage, sputtering targets, target pulse duration and sequence, and other parameters.

#### Acknowledgements

This work was supported in part by the A\*STAR, Singapore, the Australian Research Council, the University of Sydney, the Lee Kuan Yew Foundation, Chartered Semiconductors Mfg., and the International Research Network for Deterministic Plasma-Aided Nanofabrication. Assistance of W. Luo, E.L. Tsakadze, Z.L. Tsakadze, and P.P. Rutkevych with the LP, OES, and QMS plasma diagnostics is kindly appreciated.

#### References

- [1] Oehrlein GS. Plasma processing of electronic materials. Berlin: Springer; 2003.
- [2] Vladimirov SV, Ostrikov K. Phys Rep 2004;393:175.
- [3] Grill A. Cold plasma in materials fabrication: from fundamentals to applications. NY: IEEE Publ; 1994.
- [4] Auciello O, Gras-Marti A, Valles-Abarca JA, Flamm DL. Plasma-surface interactions and processing of materials. Boston: Kluwer; 1990.
- [5] Ostrikov K. Rev Mod Phys 2005;77:489.
- [6] Xu S, Ostrikov KN, Li YA, Tsakadze EL, Jones IR. Phys Plasma 2001;8:2459.
- [7] Denysenko IB, Ostrikov K, Xu S, Yu MY, Diong CH. J Appl Phys 2003;94:6097.
- [8] Ostrikov K, Denysenko IB, Vladimirov SV, Xu S, Sugai H, Yu MY. Phys Rev E 2003;67:056408/1–13.
- [9] Denysenko IB, Xu S, Long JD, Rutkevych PP, Azarenkov NA, Ostrikov K. J Appl Phys 2004;95:2713.
- [10] Ostrikov KN, Xu S, Shafiu Azam ABM. J Vac Sci Technol A 2002;20:251.
- [11] Tsakadze EL, Ostrikov K, Tsakadze ZL, Vladimirov SV, Xu S. Phys Plasmas 2004;11:3915.
- [12] Lieberman MA, Lichtenberg AJ. Principles of plasma discharges and materials processing. New York: Wiley; 1994.
- [13] Tsakadze EL, Ostrikov K, Tsakadze ZL, Xu S. J Appl Phys 2005;97:013301/1–10.
- [14] Chan M, Xu S, Jiang N, Long J, Diong CH. Int J Mod Phys B 2002;16:254.
- [15] Long JD, Xu S, Lu JH, Ostrikov KN, Diong CH. IEEE Trans Plasma Sci 2002;30:118.

- [16] Chua HL, Xu S. 2nd international conference on nanostructures and nanotechnology, 25–26 November 2004, Singapore. Contributed Paper T18.
- [17] Levchenko I, Ostrikov K, Keidar M, Xu S. *J Appl Phys* 2005;98, to be published.
- [18] Tsakadze ZL, Ostrikov K, Xu S. *Surf Coat Technol* 2004;191/1:49.
- [19] Tsakadze ZL, Ostrikov K, Long JD, Xu S. *Diam Relat Mater* 2004;13:1923.
- [20] Long JD, Xu S, Cai JW, Jiang N, Lu JH, Ostrikov KN, Diong CH. *Mat Sci Eng C* 2002;20:175.
- [21] Xu S, Long JD, Sim L, Diong CH, Ostrikov K. *Plasma Proc Polym* 2005;2:373.